

Title	Origin of the visible-light response of nickel(II) oxide cluster surface modified titanium(IV) dioxide
Authors	Iwaszuk, Anna;Nolan, Michael;Jin, Qiliang;Fujishima, Musashi;Tada, Hiroaki
Publication date	2013-01-24
Original Citation	Iwaszuk, A., Nolan, M., Jin, Q., Fujishima, M. and Tada, H. (2013) 'Origin of the Visible-Light Response of Nickel(II) Oxide Cluster Surface Modified Titanium(IV) Dioxide', The Journal of Physical Chemistry C, 117(6), pp. 2709-2718. doi: 10.1021/jp306793r
Type of publication	Article (peer-reviewed)
Link to publisher's version	http://pubs.acs.org/doi/abs/10.1021/jp306793r - 10.1021/jp306793r
Rights	© 2013 American Chemical Society. This document is the Accepted Manuscript version of a Published Work that appeared in final form in The Journal of Physical Chemistry C, copyright © American Chemical Society after peer review and technical editing by the publisher. To access the final edited and published work see http://pubs.acs.org/doi/abs/10.1021/jp306793r
Download date	2024-04-17 19:31:59
Item downloaded from	https://hdl.handle.net/10468/1595



UCC

University College Cork, Ireland
Coláiste na hOllscoile Corcaigh

Origin of the Visible-Light Response of Nickel(II) Oxide Cluster Surface Modified Titanium(IV) Dioxide

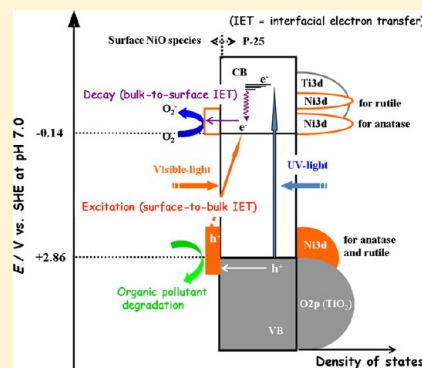
Anna Iwaszuk,[†] Michael Nolan,^{*,†} Qiliang Jin,[‡] Musashi Fujishima,[‡] and Hiroaki Tada^{*,‡}

[†]Tyndall National Institute, University College Cork, Lee Maltings, Prospect Row, Cork, Ireland

[‡]Department of Applied Chemistry, School of Science and Engineering, Kinki University, 3-4-1, Kowakae, Higashi-Osaka, Osaka 577-8502, Japan

Supporting Information

ABSTRACT: A number of NiO clusters have been formed on TiO₂ (anatase/rutile = 4/1 w/w, P-25, Degussa) in a highly dispersed state (NiO/TiO₂) by the chemisorption–calcination cycle technique. The NiO/TiO₂ causes high visible-light activities for the degradations of 2-naphthol and *p*-cresol exceeding those of FeO_x/TiO₂ (Tada et al. *Angew. Chem., Int. Ed.* **2011**, *50*, 3501–3505). The main purpose of this study is to clarify the origin at an electronic level by the density functional simulation for NiO, Ni₂O₃, and Ni₄O₄ clusters supported on TiO₂ rutile (110) and anatase (001) surfaces. The clusters adsorb strongly on both rutile and anatase with adsorption energies ranging from –3.18 to –6.15 eV, creating new interfacial bonds between the clusters and both surfaces. On rutile, intermetallic Ni–Ti bonds facilitate stronger binding compared with anatase. The electronic structure shows that the top of the valence bands (VBs) of rutile and anatase arises from electronic states on the NiO cluster. On the other hand, the conduction band of rutile is from the Ti 3d states, whereas NiO cluster levels are generated near the conduction band minimum of anatase. This is in contrast to the SnO₂/rutile TiO₂ system, where the density of states near the conduction band minimum increases with the VB unmodified. In the NiO/TiO₂ system, the band gaps of both rutile and anatase are narrowed by up to 0.8 eV compared with pristine TiO₂, which pushes the photoactivity into the visible region. In view of the calculated electronic structure, we have attributed the enhanced photocatalytic activity both to the charge separation due to the excitation from the Ni 3d surface sub-band to the TiO₂ conduction band and the action of the NiO species as a mediator for the electron transfer from the TiO₂ conduction band to O₂.



1. INTRODUCTION

One of the biggest challenges for our energy security is to be independent of fossil fuels, and the development of suitable photocatalysts may help in solar energy harvesting. TiO₂ has gathered much attention because it is relatively cheap, readily available, stable, and nontoxic. Since TiO₂ absorbs only in the ultraviolet region, there have been many attempts to modify it in such a way that it will also absorb visible light.^{1,2} A popular approach for material modification over many years has been substitutional cation or anion doping at titanium or oxygen sites.^{3–19} In 2001, Asahi et al. demonstrated that N-doping of TiO₂ results in visible light absorption,³ and there has been much work since devoted to examining doping as a means to shifting the band gap of TiO₂ from the UV to the visible. N-doped TiO₂ continues to be of great interest and has been studied in depth by Di Valentin, Pacchioni, and Selloni in refs 4 and 5, while there have been recent experimental and modeling reports on this prototype of doped TiO₂.^{6,7} Carbon-doped TiO₂ has also been of great interest,^{8–11} while Wang and Lewis have used the FIREBALL code to study doping of TiO₂^{12,13} and obtained results that were used to explain the band gap changes in doped TiO₂. Finally, other studies of doped TiO₂ in

refs 14–19 serve to highlight the range of dopants that have been studied.

It has been highlighted that there are practical questions associated with doping of TiO₂, including solubility, stability, determining that doping has actually taken place, and charge recombination.^{20,21} Herrmann has shown that Cr-doping of TiO₂, which does reduce the band gap, will in fact have a detrimental effect on the photocatalytic activity.²² With this in mind, there have been many efforts to find alternative ways to shift the band gap of TiO₂ in order to make it more efficient in terms of visible-light absorption and reducing charge recombination. This includes modification with metal particles, such as gold,²¹ modification with quantum dots, for example, CdS²³ (which, although displaying an initially high photocatalytic efficiency, does subsequently degrade as a result of CdS oxidation), and heterostructures of graphene and TiO₂.²⁴

Recent studies have demonstrated that oxide–oxide heterostructures composed of nanoscale metal oxide clusters on TiO₂ can drastically improve the photocatalytic properties

Received: July 9, 2012

Revised: January 23, 2013

68 compared to pure TiO₂.^{25–31} Modification of TiO₂ with metal
69 oxide nanoclusters has been investigated by Libera et al.²⁹ and
70 Tada et al.^{30,31} Libera et al. used the atomic layer deposition
71 technique to deposit Fe₂O₃ nanoclusters on TiO₂ and found
72 visible-light absorption and efficient photocatalytic degradation
73 of methylene blue.²⁹ Tada et al. synthesized FeO_x-modified
74 TiO₂ using the chemisorption–calcination cycle (CCC) that
75 deposits highly dispersed metal oxide nanoclusters on the TiO₂
76 surface at a molecular scale.³⁰ The FeO_x/TiO₂ structure shows
77 improved visible-light activity and also good UV-light activity.
78 These features came from band gap narrowing and were
79 explained by the presence of the FeO_x clusters that are
80 responsible for shifting the valence band (VB) maximum of
81 TiO₂.³¹ Further, with SnO₂-modified TiO₂, striking differences
82 between the light absorption properties and the visible-light
83 photocatalytic activity of modified rutile and anatase TiO₂ were
84 observed and rationalized with first-principles simula-
85 tions.^{32,33} Other examples of heterostructures have included
86 BiOBr–ZnFe₂O₄,²⁷ BiVO₄–WO₃,²⁸ SnO_x–ZnGa₂O₄,³⁴ and
87 AgI–BiO,³⁵ displaying improved photocatalytic activity com-
88 pared to the pure oxides or simple physical mixtures,
89 highlighting the important role of the interface.³⁵ Further, the
90 Ni²⁺ surface modification of rutile TiO₂ by the impregnation
91 method was reported to enhance both the UV- and visible-light
92 activities, whereas the effect is much smaller than that by the
93 Fe³⁺ surface modification.³⁶ Recently, we have shown that the
94 surface modification of TiO₂ with extremely small NiO clusters
95 by the CCC technique (NiO/TiO₂) causes a high visible-light
96 activity concomitantly with the UV-light activity increased for
97 the decomposition of 2-naphthol.³⁷ However, the origin of the
98 visible-light response is not fully understood and needs further
99 investigation to facilitate the development of this exciting
100 approach to developing photocatalytic materials.

101 On the other hand, to understand the origin of the
102 experimental findings, density functional theory (DFT)
103 simulations are of great help. Iwaszuk and Nolan have shown
104 that that subnanometer diameter (TiO₂)_n clusters, with $n = 2–$
105 4, adsorbed on the rutile TiO₂(110) surface, can reduce the
106 band gap compared to pure TiO₂ (although that work was also
107 focused on examining the reactivity of these heterostruc-
108 tures).³⁸ The presence of Ti 3d states of the cluster above the
109 VB will enhance charge separation, and the photocatalytic
110 activities will be improved.³⁸ Moreover, further work has
111 demonstrated that modification of TiO₂ with other transition
112 metal oxides will also result in potentially useful photocatalytic
113 properties. For example, DFT simulations show that small
114 transition metal oxide nanoclusters, for example, Cr₂O₃ and
115 Mo₂O₄, deposited on TiO₂ rutile (110) will lead to a band gap
116 reduction³⁹ and improvement of photocatalytic activities. Thus,
117 the surface modification of the catalyst is an approach that may
118 benefit over doping by reducing formation of localized
119 electronic states and electron/hole recombination that are the
120 key factors for an efficient photocatalyst.

121 Herein, we report that NiO/TiO₂ (anatase/rutile = 4/1 w/w,
122 specific surface area = 50 m² g^{−1}, P-25, Degussa) exhibits high
123 levels of visible-light activities for 2-naphthol and *p*-cresol
124 degradations concurrently with enhanced UV-light activity. P-
125 25 possesses high UV-light activity for the degradation of most
126 organic compounds. Furthermore, in elucidating the origin of
127 the activity of NiO-modified TiO₂, we show by spectroscopic
128 measurements and DFT calculations that the visible-light
129 response of modified TiO₂ is induced by the rise in the VB top
130 with NiO surface modification. We investigate the TiO₂ anatase

(001) and rutile (110) surfaces modified with NiO nanoclusters
131 using DFT simulations to establish (1) how NiO nanocluster
132 modification of TiO₂ changes the light absorption properties
133 and (2) if there is any sensitivity to TiO₂ crystal form, as
134 observed for SnO₂.³³ We investigated representative structures
135 of NiO, Ni₂O₃, and Ni₄O₄ nanoclusters deposited on both
136 TiO₂ surfaces. All NiO clusters adsorb strongly on both
137 surfaces; however, adsorption is stronger at the rutile (110)
138 surface due to formation of additional Ni–Ti metallic bonds
139 that are not possible at the anatase (001) surface. The
140 electronic structure shows that the band gap is narrowed and
141 the energy band alignments will give electron and hole
142 separation after light excitation. 143

2. METHODOLOGY

2.1. Photocatalyst Synthesis. The NiO/P-25 was
144 prepared by the CCC technique.³⁰ After P-25 (1 g) had been
145 added to 100 mL of a Ni(acac)₂(H₂O)₂ solution (solvent,
146 ethanol/*n*-hexane = 3:17 v/v), they were allowed to stand for
147 24 h at 298 K. The Ni(acac)₂(H₂O)₂ concentration was
148 changed ranging from 1 × 10^{−5} to ~5 × 10^{−3} M. The resulting
149 samples were washed repeatedly with the solvent for the
150 physisorbed complexes to be removed and dried, followed by
151 heating in air at 773 K for 1 h. The complex adsorption and the
152 subsequent heating were repeated to increase the Ni loading
153 amount. The loading amount was shown by the amount of Ni
154 loaded on the unit surface area of P-25 (Γ, ions nm^{−2}). 155

2.2. Photocatalyst Characterization. High-resolution
156 transmission electron microscopy (HRTEM) observation and
157 X-ray energy dispersive spectroscopic measurements were
158 performed using a JEOL JEM-3000F and a Gatan imaging
159 filter at an applied voltage of 300 or 297 kV. UV–visible diffuse
160 reflectance spectra of NiO/TiO₂ were recorded on a Hitachi U-
161 4000 spectrophotometer. The spectra were converted to the
162 absorption spectra by using the Kubelka–Munk function. X-ray
163 photoelectron spectroscopic (XPS) measurements were
164 performed using a Kratos Axis Nova X-ray photoelectron
165 spectrometer with a monochromated Al Kα X-ray source ($h\nu =$
166 1486.6 eV) operated at 15 kV and 10 mA. The takeoff angle
167 was 90°, and multiplex spectra were obtained for Ni 2p, O 1s,
168 and Ti 2p photopeaks. All the binding energies were referenced
169 with respect to the C 1s at 284.6 eV. The photoluminescence
170 spectra were measured with an excitation wavelength of 320 nm
171 at 77 K using a JASCO FP-6000 spectrofluorometer. 172

2.3. Photocatalytic Reactions. A 50 mL amount of 1.0 ×
173 10^{−5} M 2-naphthol solution (solvent, acetonitrile/water = 1:99
174 v/v) or 5.0 × 10^{−4} M *p*-cresol solution (solvent, water) was
175 placed in a double-jacket-type reaction cell made of borosilicate
176 glass, and then, P-25 (Degussa) or NiO/P-25 particles (0.1 g)
177 were added. The reaction cell was irradiated with a Xe lamp
178 (Wacom XRD-501SW) through a band-pass filter (33U,
179 SIGMA KOKI CO., Ltd.) superposed on FTO-coated glass
180 (two pieces of FTO glass for 2-naphthol and a piece of FTO
181 glass for *p*-cresol) transmitting only the 330–400 nm range for
182 the UV-light photocatalytic activity evaluation and a high-pass
183 filter (L-42, Toshiba) to cut off UV light for the visible-light-
184 induced activity test. The irradiation conditions are as follows:
185 for 2-naphthol UV light, 330 < λ < 400 nm, I_{320–400 nm} = 0.5
186 mW cm^{−2}, and visible light, λ > 400 nm, I_{420–485 nm} = 1.0 mW
187 cm^{−2}; for *p*-cresol UV light, 330 < λ < 400 nm, I_{320–400 nm} = 2
188 mW cm^{−2}, and visible light, λ > 400 nm, I_{420–485 nm} = 2 mW
189 cm^{−2}. A 3 mL amount of the solution was sampled every 15
190 min, and the absorbance at λ = 224 nm was measured using a 191

192 spectrometer (UV-1800, Shimadzu) to determine the concen-
193 tration of 2-naphthol. The *p*-cresol concentration was
194 determined by high-performance liquid chromatography
195 (SPD-6A, Shimadzu; column = Fluofix INW425 4.6 mm ×
196 250 mm (NEOS); mobile phase = water–ethanol (3:7 v/v); λ
197 = 277 nm).

198 **2.4. DFT Simulation.** For modeling TiO₂ rutile (110) and
199 anatase (001) surfaces, we use three-dimensional periodic slab
200 models with the VASP code.⁴⁰ The valence electrons are
201 described by a plane wave basis set, and the cutoff for kinetic
202 energy is 396 eV. The valence electrons are 4 for Ti, 6 for O,
203 and 10 for Ni, within the PAW approximation, and the
204 exchange–correlation functional is the approximation of
205 Perdew–Wang (PW91).^{41,42} The Monkhorst–Pack scheme is
206 used for k-point sampling with a (2 × 2 × 1) sampling grid.
207 The rutile (110) surface is terminated by 2-fold coordinated
208 bridging oxygen atoms, and the next sublayer consists of 6-fold
209 and 5-fold coordinated Ti atoms. The (unreconstructed) (001)
210 surface model of anatase is terminated by 2-fold coordinated
211 oxygen and has 5-fold coordinated Ti ions in the next sublayer.
212 We use models of rutile (110) and anatase (001), since (110) is
213 by far the most stable surface of rutile and is well studied,⁴³
214 while for anatase, (001) is of great interest as the most
215 photocatalytically active anatase surface.^{44,45} We consider the
216 rutile and anatase surfaces in their perfect, stoichiometric form,
217 with consideration of the OH-terminated surfaces that are well
218 known for TiO₂ being the subject of ongoing studies. In order
219 to have isolated NiO nanoclusters, we employed a (2 × 4)
220 surface supercell for each TiO₂ surface; for the largest NiO
221 nanocluster considered, a (4 × 4) rutile (110) surface was also
222 studied to examine the effect of the interaction of NiO clusters
223 with periodic images on the resulting properties, with the larger
224 surface supercell giving a bigger distance between periodic NiO
225 images, thus reducing the periodic interactions and modeling
226 more widely separated NiO nanoclusters. NiO nanoclusters
227 with composition NiO, Ni₂O₂, Ni₃O₃, and Ni₄O₄ are studied as
228 representative molecular-sized NiO nanoclusters. The super-
229 cells and technical parameters for the free nanoclusters are the
230 same as the extended surfaces.

231 For the calculations we use the DFT+*U* approach^{46,47} where
232 we applied *U* = 4.5 eV on the Ti 3d states. The need to
233 introduce the *U* parameter in order to describe properly
234 electronic states of d or f shells is well known.^{46–50} We also
235 applied the +*U* correction for Ni in NiO, since the electronic
236 states of NiO are known to be poorly described with
237 DFT;^{46,47,51–53} for Ni, we apply *U* = 8 eV and *J* = 1 eV (giving
238 *U* – *J* = 7 eV), generally consistent with values from the
239 literature, for example, refs 51–53; a check with other values of
240 *U*, namely, (*U* – *J*) = 5 and 6 eV, gives similar results to those
241 found here for the electronic structure. The DFT+*U* approach
242 gives a reasonable description of transition metal d states, but
243 still an underestimation of band gap remains, and this depends
244 on the precise DFT+*U* setup. With this in mind, the change in
245 the band gap of TiO₂ upon modification with NiO, which is
246 more reliable, is our primary focus.

247 The clusters were deposited on both TiO₂ surfaces and fully
248 relaxed. The adsorption energy was computed from the
249 following:

$$E^{\text{ads}} = E((\text{NiO})_n - \text{TiO}_2) - \{E((\text{NiO})_n) + E(\text{TiO}_2)\} \quad (1)$$

251 where $E((\text{NiO})_n - \text{TiO}_2)$ is the total energy of the NiO
252 nanocluster supported on the surface and $E((\text{NiO})_n)$ and

$E(\text{TiO}_2)$ are the total energies of the free cluster and the bare
253 surface, respectively. A negative adsorption energy signifies that
254 the cluster adsorption is stable. 255

3. RESULTS

The point of effective surface modification of TiO₂ with metal
256 oxide clusters is the dispersion state and the strict control of the
257 loading amount.³⁰ The Ni(acac)₂(H₂O)₂ complex is chem-
258 isorbed on P-25 via the partial ligand exchange between the
259 acac ligand and the acidic surface Ti–OH group to yield NiO
260 clusters by postheating.³⁷ Figure 1 shows HRTEM micrographs
261 of

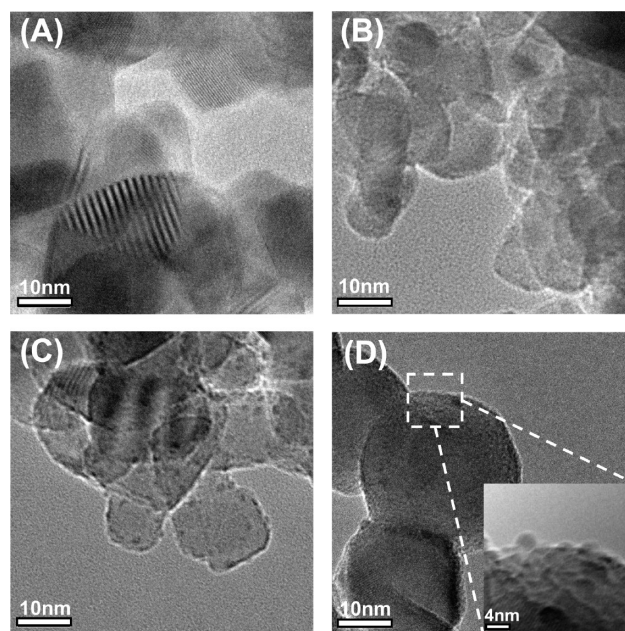


Figure 1. HRTEM images of NiO/P-25: (A) $\Gamma = 0$; (B) $\Gamma = 0.014$;
(C) $\Gamma = 0.47$; (D) $\Gamma = 0.83$.

of NiO/TiO₂ with varying Ni loading amount Γ (ions nm⁻²).
262 Highly dispersed NiO clusters smaller than ~2 nm are observed
263 on the surface of P-25. The strong chemisorption of the
264 complex on the TiO₂ surface (DFT results) prevents
265 aggregation of the small NiO clusters into larger structures
266 during the subsequent heating, thus yielding extremely small
267 adsorbed NiO clusters. 268

2-Naphthol and *p*-cresol were used as model water
269 pollutants. 2-Naphthol, a starting material of azo-dyes, has no
270 absorption at $\lambda > 330$ nm.⁵⁴ Both the degradations of 2-
271 naphthol and *p*-cresol apparently followed the first-order rate
272 law under irradiation of UV light and visible light, and the
273 activity was evaluated by the pseudofirst-order rate constant (*k*,
274 h⁻¹). Figure 2A (red circles) shows visible-light activity for the
275 2-naphthol degradation as a function of Γ . The surface
276 modification with NiO clusters endows P-25 with visible-light
277 activity, whereas pristine P-25 has only low activity. The visible-
278 light activity drastically increases with increasing Γ , passing
279 through a maximum at $\Gamma \sim 0.32$. The maximum activities of
280 several metal oxide surface modified P-25 are on the order of
281 NiO > FeO_x > SnO₂ > none under the same reaction
282 conditions, and the value of NiO/P25 reaches approximately
283 twice that of the FeO_x/P-25 system (Table S1, Supporting
284 Information).³⁰ Figure 2B (red circles) shows UV-light activity
285 for the 2-naphthol degradation as a function of Γ . The UV-light
286 activity further increases by the surface modification with the
287

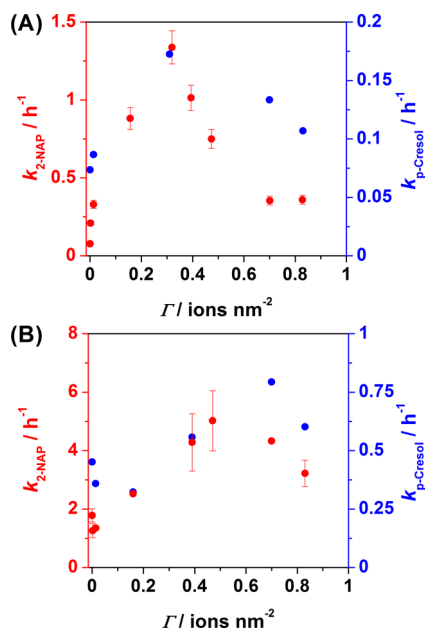


Figure 2. (A) Visible-light and (B) UV-light activities of NiO/P-25 for 2-naphthol (red circles) and *p*-cresol (blue circles) degradations.

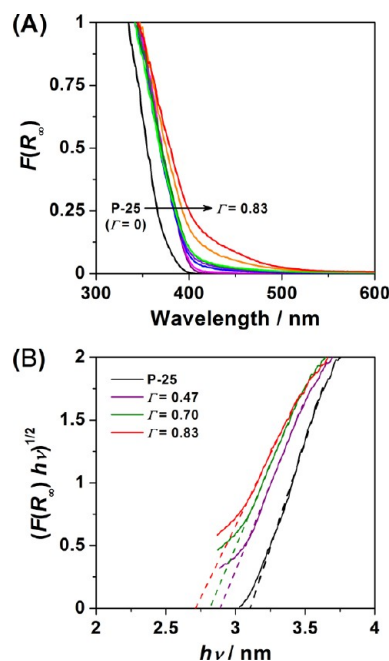


Figure 3. (A) UV–visible absorption spectra of NiO/P-25 with varying Γ : $F(R_\infty)$ denotes the Kubelka–Munk function. (B) Plots of $(F(R_\infty)h\nu)^{1/2}$ vs $h\nu$.

288 NiO clusters. The loading at $\Gamma = 0.47$ affords a maximum
 289 activity, which is ~ 2.8 times the activity of P-25. The maximum
 290 activities of several metal oxide surface modified P-25 are on
 291 the order of $\text{FeO}_x > \text{NiO} > \text{SnO}_2 \sim \text{none}$ (Table S1,
 292 Supporting Information). We have recently reviewed the
 293 difference in the surface modification effect between FeO_x
 294 and SnO_2 clusters.⁵⁵ On the other hand, *p*-cresol widely used as
 295 a sterilizer and disinfectant has no absorption at $\lambda > 330$ nm. As
 296 shown in Figure 2A,B (blue circles), similar trends are also
 297 observed for the degradation of *p*-cresol, while the enhance-
 298 ment effect is somewhat smaller as compared to that for the 2-
 299 naphthol degradation.

300 The effect of the surface modification of P-25 with varying
 301 amounts of NiO clusters on the optical property was studied.
 302 Ni-doped TiO_2 prepared by the solid-state reaction of TiO_2
 303 with NiO has a broad and weak absorption around 450 nm due
 304 to the d–d transition, while the intrinsic absorption edge is
 305 invariant.⁵⁶ Chemical doping of Cr and N ions into TiO_2 yields
 306 similar weak shoulders in the visible region due to the
 307 formation of localized impurity levels within the band gap.⁵⁷
 308 Figure 3A shows UV–visible absorption spectra of NiO/P-
 309 25 with varying Γ : $F(R_\infty)$ is the Kubelka–Munk function. In
 310 contrast to the spectra of Ni-doped TiO_2 , band gap narrowing
 311 occurs for NiO/P-25, whereas the d–d transition band grows at

312 $\Gamma > 0.47$. Figure 3B shows plots of $[F(R_\infty)h\nu]^{1/2}$ versus $h\nu$ for
 313 NiO/P-25.⁵⁸ The indirect band gap determined from the
 314 extrapolation of the tangent to the abscissa decreases from 3.1
 315 eV at $\Gamma = 0$ to 2.6 eV at $\Gamma = 0.83$. A similar spectral feature is
 316 observed for Cr-⁵⁹ and N-doped⁶⁰ TiO_2 prepared by physical
 317 techniques such as ion implantation and magnetron sputtering.
 318 Also, the VB-XPS was measured for NiO/P-25 with varying Γ .
 319 As shown in Figure 4A, the emission from the VB extends from
 320 2 to 9 eV for every sample. Figure 4B magnifies the energy
 321 region near the VB maximum. The top of the VB rises with an
 322 increase in Γ . The magnitude of the change reaches
 323 approximately 0.5 eV at $\Gamma = 0.83$, which is comparable with
 324 the decrement in the band gap with the surface modification.
 325 Consequently, the visible-light absorption of TiO_2 by the

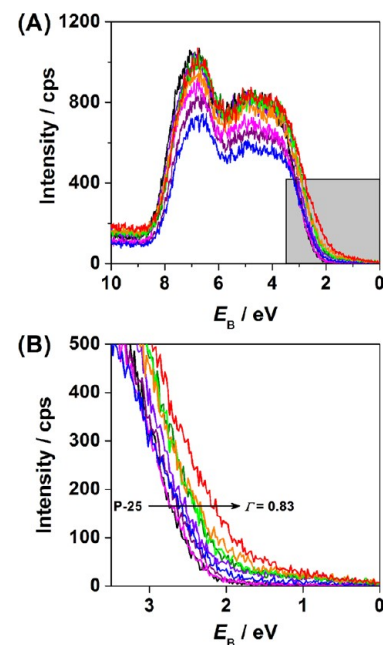


Figure 4. (A) VB-XPS of NiO/P-25 ($\Gamma = 0, 0.0018, 0.014, 0.16, 0.32, 0.39, 0.47, 0.70, \text{ and } 0.83$ from left to right). (B) Magnified VB-XPS near the VB maximum.

surface modification with the NiO clusters stems from the rise
 in the top of the VB.

To understand the effect of the surface modification with the
 NiO clusters at an electronic level, DFT simulations were
 performed for model systems consisting of TiO_2 and NiO
 nanoclusters adsorbed at rutile and anatase. Figure 5 presents
 the atomic structure of the NiO, Ni_2O_2 , Ni_3O_3 , and Ni_4O_4
 nanoclusters, which are chosen as representative NiO nano-
 clusters, adsorbed on TiO_2 anatase (001) and rutile (110)
 surfaces together with the adsorption energies and the

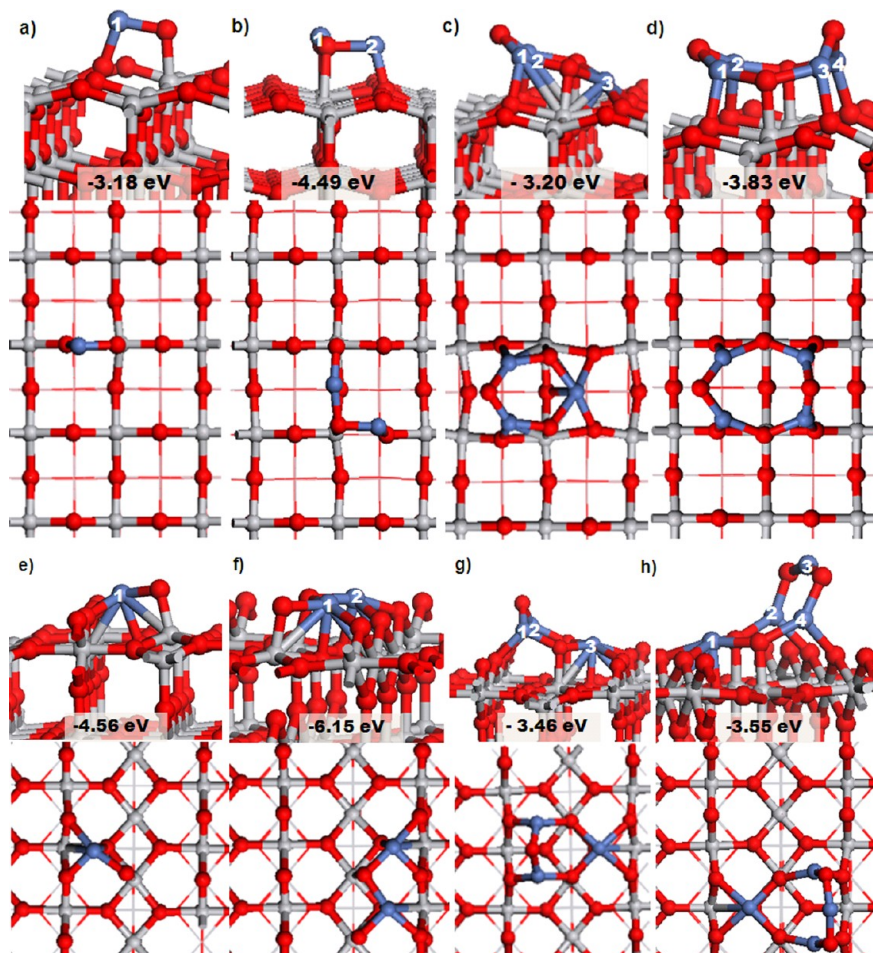


Figure 5. Relaxed adsorption structures with adsorption energies given in eV for (a) NiO, (b) Ni₂O₂, (c) Ni₃O₃, and (d) Ni₄O₄ clusters on TiO₂ anatase (001) and (e) NiO, (f) Ni₂O₂, and (g) Ni₃O₃ clusters on TiO₂ rutile (110). The blue spheres are Ni atoms, the gray spheres are Ti atoms, and the red spheres are O atoms. Cluster Ni atoms are numbered.

336 numbering of the nanocluster Ni atoms. We compute the
 337 coverage of the nanoclusters in terms of Ni atoms per unit area,
 338 so that for NiO, Ni₂O₂, Ni₃O₃, and Ni₄O₄ on anatase (001), the
 339 coverages are 0.85, 1.70, 2.55, and 3.41 Ni atoms/nm². On
 340 rutile (110), the corresponding coverages are 0.64, 1.28, 1.92,
 341 and 2.56 Ni atoms/nm². On the larger (4 × 4) surface
 342 supercell, the coverage is 1.28 Ni atoms/nm². For Ni₄O₄, the
 343 size of the nanocluster on a (2 × 4) surface supercell will lead
 344 to stronger periodic NiO–NiO interactions than for the smaller
 345 NiO nanoclusters, which will influence the adsorption structure,
 346 due to the NiO nanoclusters being essentially in close
 347 proximity, and the effect of this on the change in the electronic
 348 properties of NiO-modified TiO₂ will be discussed.

349 All structures show negative adsorption energies, ranging
 350 from –3.18 to –6.15 eV giving an indication of a strong
 351 interaction between the nanocluster and the surface and the
 352 high stability of individual NiO nanoclusters adsorbed at TiO₂,
 353 which prevents aggregation of the clusters into larger structures
 354 during postheating. For all deposited clusters, detailed
 355 information about the geometry is presented in Table 1.

356 For NiO nanoclusters deposited on anatase, the NiO cluster
 357 results in two new bonds with the TiO₂ surface with distances
 358 of 1.75 and 1.91 Å. It is important to note that an O atom from
 359 the anatase surface is pulled out of the surface by Ni from the
 360 cluster by 0.26 Å that distorts the surface of TiO₂ anatase
 361 (001), similar to SnO₂ adsorbed at anatase (001).³² The same

behavior is observed for Ni₂O₂ deposited at anatase (001),³⁶²
 where in this case the O atom is pulled out of the surface by
 363 0.17 Å upon bonding to Ni. The number of new bonds in
 364 Ni₂O₂ deposited on TiO₂ anatase (001) is three. The Ni₃O₃
 365 cluster presents 11 new bonds when deposited on TiO₂ anatase
 366 (001). There are five bonds between Ni and O atoms in the
 367 range 1.93–2.20 Å while oxygen atoms from the cluster bond
 368 to Ti surface atoms with two bonds that are 1.90 Å long. The
 369 Ni₄O₄ cluster deposited on TiO₂ anatase (001) shows six new
 370 bonds. In this case, the surface O atom is pulled out of the
 371 surface by 0.19 Å. Within the Ni–O nanoclusters, the Ni–O
 372 distances are notably shorter compared to bulk NiO, for
 373 example, 1.95 Å in Ni₄O₄, compared to 2.10 Å in bulk NiO. Of
 374 the NiO nanoclusters adsorbed at anatase (001), only the
 375 Ni₃O₃ nanocluster shows intermetallic Ni–Ti bonds, with Ni–
 376 Ti distances in the range 2.71–2.87 Å, which is consistent with
 377 those in the intermetallic NiTi alloy.⁶¹ 378

At the TiO₂ rutile (110) surface, the NiO cluster bonds to
 379 the surface with six new bonds. The Ni atom from the cluster
 380 bonds with two bridging O atoms and one surface O atom, and
 381 the fourth metal–oxygen bond is from an O cluster atom that
 382 bonds to Ti surface atoms. The Ni₂O₂ cluster binds to the
 383 surface with nine new bonds. Five metal–oxygen bonds are
 384 from Ni cluster atoms to surface oxygen, and the last two are
 385 from cluster oxygen to surface Ti. Ni₃O₃ deposition on rutile
 386 (110) results in formation of seven new bonds between the
 387

Table 1. Surface–Cluster Ni–O Bond Distances for NiO Clusters Adsorbed at the TiO₂ Anatase (001) and Rutile (110) Surfaces^a

	distance (Å)					
	anatase			rutile		
	Ni _c –O _s	O _c –Ti _s	Ni _c –Ti _s	Ni _c –O _s	O _c –Ti _s	Ni _c –Ti _s
NiO	1.75 (1)	1.91		2.08 (1)	1.80	2.61 (1)
				1.96 (1)		2.81 (1)
				2.03 (1)		
Ni ₂ O ₂	1.73 (2)	1.99		2.10 (1)	1.96	2.79 (1)
		2.22		1.92 (1)	1.78	2.70 (1)
				2.09 (1)		2.58 (2)
				2.02 (2)		
				2.03 (2)		
Ni ₃ O ₃	1.95 (1)	1.90	2.87 (1)	1.97 (1)	1.89	2.73 (3)
	1.93 (2)	1.90	2.85 (2)	1.96 (2)	1.89	2.87 (3)
	2.07 (3)		2.71 (3)	2.20 (3)		2.87 (3)
	2.02 (3)		2.71 (3)	2.20 (3)		
	2.20 (3)			2.05 (3)		
Ni ₄ O ₄	1.95 (1)	1.93		2.21 (1)	1.89	2.74 (1)
	1.92 (2)	1.92		2.22 (1)	1.90	
	1.95 (3)			2.04 (1)		
	1.95 (4)			1.96 (2)		
			1.99 (4)			

^aThe numbers in parentheses are the atom numbers of Ni in each NiO nanocluster.

cluster and surface. Five bonds are between Ni cluster atoms and surface O atoms with the bond distances from 1.96 to 2.20 Å. The other two bonds come from O cluster atoms and Ti surface atoms, and their distance is 1.89 Å. The Ni₄O₄ cluster bonds to the rutile surface with eight new bonds where three of the cluster Ni atoms create four Ni–O bonds with bridging surface O atoms and one surface O atom, with the shortest distance being 1.96 Å and the longest distance being 2.22 Å. The other two bonds are from cluster O binding with surface Ti. In each of these structures, surface Ti atoms are pulled out of the surface after bonding to cluster oxygen. For the example of NiO adsorbed at rutile (110), this Ti is displaced by 0.48 Å. At the (110) surface, we also observe the formation of new intermetallic Ni–Ti bonds between cluster Ni and surface Ti, with the distances given in Table 1. The Ni–Ti distances we observe are consistent with those in the intermetallic NiTi alloy.⁶¹ Since the adsorption energies of NiO nanoclusters on the rutile (110) surface are more negative compared to those on anatase (001) for a given NiO cluster, we suggest that the presence of the new Ni–Ti bonds plays a role in further stabilization of the heterostructure. The exception is the Ni₃O₃ nanocluster, where Ni–Ti bonds are formed at both TiO₂ surfaces and the adsorption energies are very similar.

Figure 6 shows the electronic density of states projected (PEDOS) on Ni 3d and Ti 3d states for NiO, Ni₃O₃, Ni₂O₂, and Ni₄O₄ clusters adsorbed on anatase (001) (Figure 6a–d) and rutile (110) (Figure 6e–h). PEDOS plots for the O 2p states are shown in the Supporting Information (Figure S1); the Ni 3d states lie near the top of the VB in the clusters and are important in this analysis. The DOS of the clean rutile and anatase TiO₂ surfaces (see the Supporting Information) show the well-known O 2p derived VB, with a Ti 3d contribution, while the conduction band is dominated by the Ti 3d states in both anatase and rutile.

Examination of the PEDOS shows clearly that, upon modification of TiO₂ with NiO nanoclusters, NiO cluster derived states are found laying above the top of the VB edge of the rutile and anatase surfaces, which pushes the VB edge of the composite system to higher energy compared to the bare surfaces. The conduction band of the NiO-modified surfaces can show some dependence on the crystal form of TiO₂. For modified rutile (110), the bottom of the conduction band is dominated by surface Ti 3d states. Interestingly, this is in contrast to the SnO₂/rutile TiO₂ system, where the DOS near the conduction band minimum increases, with the VB unmodified.³² A close inspection of the conduction band states for anatase indicates that, in some cases, for example, Ni₂O₂, empty NiO cluster levels are generated near the conduction band minimum.

In the NiO/TiO₂ system, the shift of the VB to higher energy has the consequence that the overall band gap of the composite is reduced compared to unmodified TiO₂. We find in the DFT calculations a maximum band gap reduction of 0.8 eV (for Ni₄O₄ at anatase (001)) compared to the unmodified anatase surface, and this shift is qualitatively comparable to the value determined by the VB-XPS, in Figure 4B. This can further be compared with SnO₂/TiO₂, where anatase modification leads to no band gap change, but rutile modification can reduce the band gap.³² The narrowing of the band gap will induce visible-light absorption in the composite as shown in Figure 3. Thus, upon modification with NiO nanoclusters, NiO states appear above the VB edge of the TiO₂ surface, which pushes the VB up in energy. There is a case in Figure 6, where the Ni₂O₂ nanocluster on anatase appears to also show some empty NiO states just below the anatase conduction band. In general, we can conclude that the NiO modification of TiO₂ will reduce the energy gap by pushing the VB edge up in energy.

We show in Figure 7 the atomic structure and PEDOS of a Ni₄O₄ nanocluster relaxed on the rutile (110) surface with a (4 × 4) surface supercell, which has a coverage of 1.28 Ni atoms/nm² and an adsorption energy of –4.50 eV. In this case, although the effect of the smaller coverage of NiO at the surface on the final adsorption structure of the nanocluster at this surface is clear compared to Figure 5f, namely, that the Ni₄O₄ cluster takes a different adsorption structure, the PEDOS shows that the impact of modifying TiO₂ with NiO is unchanged, namely, that there are NiO-derived states found at the top of the VB, which will reduce the energy gap compared to unmodified TiO₂.

The oxidation state of the metal oxide surface modifier can also affect the photocatalytic activity of TiO₂.³³ A Bader charge analysis⁶² on Ni for the NiO nanoclusters deposited on both surfaces gives net charges on Ni ranging from 8.7 to 8.9 electrons, which are consistent with a Ni²⁺ oxidation state. Moreover, in TiO₂, the computed net Bader charges are approximately +1.3 electrons, which is typical for the Ti⁴⁺ oxidation state. The oxidation states of Ni and Ti are in agreement with those determined by XPS.³⁷

On the basis of these results above, the NiO surface modification effect on the photocatalytic activity of P-25 can be rationalized as follows and indicated in Figure 8. NiO clusters possess a strong interaction with the anatase and rutile surfaces through Ni–O–Ti bonds for anatase and rutile and additional Ni–Ti bonds for rutile. As a result of the mixing of the Ni 3d levels, the VB maximum of TiO₂ rises significantly, while new vacant levels are generated near the conduction band minimum of anatase that is the major phase of P-25.

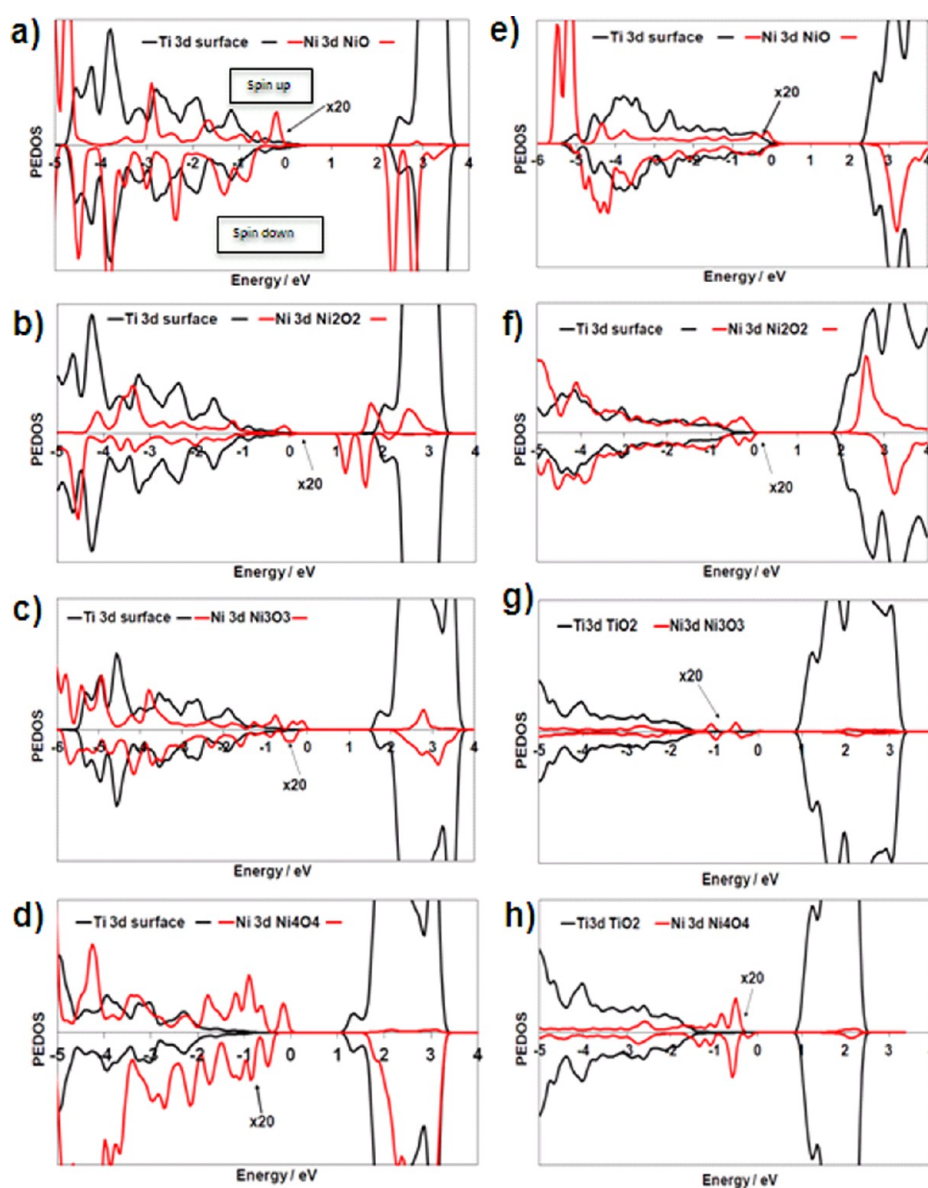


Figure 6. Spin polarized PEDOS on Ni 3d and Ti3d states for (a) NiO, (b) Ni₂O₂, (c) Ni₃O₃, and (d) Ni₄O₄ clusters supported on the anatase (001) surface and for (e) NiO, (f) Ni₂O₂, (g) Ni₃O₃, and (h) Ni₄O₄ clusters supported on the TiO₂ rutile (110) surface.

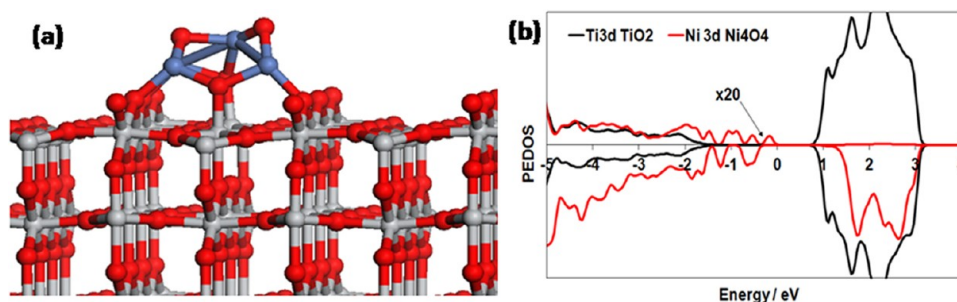


Figure 7. (a) Atomic structure and (b) PEDOS for a Ni₄O₄ cluster adsorbed at the rutile (110) surface in a (4 × 4) surface supercell.

485 Upon visible-light irradiation of NiO/P-25, the electrons in
 486 the surface Ni 3d sub-band are excited to the TiO₂ conduction
 487 band. This surface-to-bulk interfacial electron transfer (IET)
 488 enhances the charge carrier separation. The holes generated at
 489 the surface d sub-band oxidize adsorbed 2-naphthol and *p*-
 490 cresol. On the other hand, the electrons in the TiO₂ conduction

band are consumed by O₂ reduction. This process can be the
 491 key to increasing photocatalytic activity in the oxidative
 492 decomposition of organic pollutants.^{63,64} Figure 8 suggests
 493 that the excited electrons in the anatase conduction band can
 494 be transferred to the surface levels of the NiO species, which
 495 further assists the electron transfer to O₂ as previously
 496

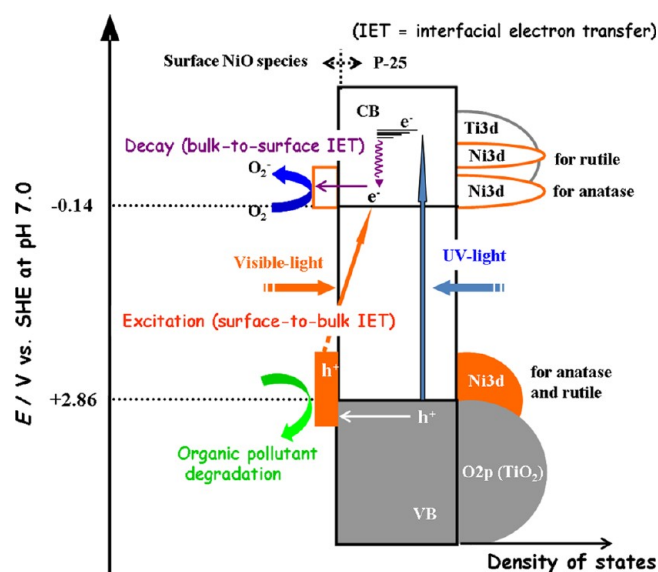


Figure 8. Energy band diagram for NiO-modified TiO₂.

497 confirmed by the electrochemical experiments.³⁷ This action
 498 mechanism of the NiO clusters should also operate under UV-
 499 light irradiation. Consequently, the NiO surface modified P-25
 500 causes the high activities under illumination of visible light and
 501 UV light. A final point is that, in the experiments, an optimum
 502 Ni loading for photocatalytic activity is found (Figure 2A,B),
 503 although above this loading, the NiO–TiO₂ system displays a
 504 continuous decrease in the band gap. With the results of this
 505 work showing that the increased loading of NiO results in a rise
 506 in the VB edge of the composite system compared to
 507 unmodified TiO₂, we can explain this finding as follows. The
 508 low VB edge in unmodified TiO₂ imparts good oxidative power
 509 to the holes formed after light excitation, while an upward shift
 510 of the VB edge will weaken the oxidation power of the holes.
 511 Thus, with an increase in NiO loading, the VB edge is shifted
 512 upward (Figures 3, 4, and 6), which therefore weakens the
 513 oxidative power of the holes and results in an optimal loading
 514 of NiO on TiO₂. A similar result has been found for other metal
 515 oxide nanocluster modified TiO₂,^{30–33} indicating that this
 516 phenomenon is quite general; that is, there will be an optimum
 517 loading of a second metal oxide on TiO₂ that shifts the VB edge
 518 such that visible-light absorption is realized but that the
 519 oxidative power of the photoexcited holes is not reduced too
 520 much.

4. CONCLUSIONS

521 We have shown that the surface modification of P-25 (anatase/
 522 rutile = 4:1 w/w) with NiO clusters gives rise to high visible-
 523 light activities for 2-naphthol and *p*-cresol concomitantly with
 524 significant increases in the UV-light activities. We have
 525 presented DFT simulations of nickel oxide clusters adsorbed
 526 on TiO₂ anatase (001) and rutile (110) surfaces to understand
 527 the origin of visible-light activity in these heterostructures. We
 528 find that NiO clusters are deposited on TiO₂ surfaces with large
 529 adsorption energies ranging from –3.18 to –6.15 eV, with
 530 metallic Ni–Ti bonds leading to extra stabilization on rutile
 531 (110) compared with anatase (001). The deposited clusters
 532 cause the narrowing of the TiO₂ band gap, which pushes the
 533 photoactivity into the visible region due to the presence of NiO
 534 states at the top of the valence band of TiO₂. The present
 535 energy level alignments enhance the charge separation and the

electron transfer to O₂, which are the origins of photocatalytic
 efficiency enhancement. These results are consistent with
 experimental data.

■ ASSOCIATED CONTENT

Supporting Information

Photocatalytic activities of metal oxide surface modified P-25
 (Degussa) for 2-naphthol degradation; Ni 3d and O 2p PEDOS
 for NiO nanocluster modified TiO₂; electronic DOS for
 unmodified rutile (110) and anatase (001) surfaces. This
 material is available free of charge via the Internet at <http://pubs.acs.org>.

■ AUTHOR INFORMATION

Corresponding Author

*E-mail: michael.nolan@tyndall.ie (M.N.); h-tada@apch.
 kindai.ac.jp (H.T.).

Notes

The authors declare no competing financial interest.

■ ACKNOWLEDGMENTS

M.N. and A.I. acknowledge support from Science Foundation
 Ireland (SFI) through the Starting Investigator Research Grant
 Program, project “EMOIN”, grant number SFI 09/SIRG/
 I1620, and computing resources at Tyndall provided by SFI
 and by the SFI and Higher Education Authority funded Irish
 Centre for High End Computing. We acknowledge support
 from the European Union through the COST Action CM1104
 “Reducible Oxide Chemistry, Structure and Functions”. H.T.
 acknowledges supports from the Ministry of Education,
 Science, Sport, and Culture, Japan through a Grant-in-Aid for
 Scientific Research (C) no. 24550239, and Nippon Sheet Glass
 Foundation for Materials Science and Engineering, and by
 Sumitomo Foundation.

■ REFERENCES

- Nie, X. L.; Zhou, S. P.; Maeng, G.; Sohlberg, K. Doping of TiO₂
 Polymorphs for Altered Optical and Photocatalytic Properties. *Int. J.*
Photoenergy **2009**, No. 294042.
- Nowotny, J. Titanium Dioxide-Based Semiconductors for Solar-
 Driven Environmentally Friendly Applications: Impact of Point
 Defects on Performance. *Energy Environ. Sci.* **2008**, *1*, 556–572.
- Asahi, R.; Morikawa, T.; Ohwaki, K.; Aoki, K.; Taga, Y. Visible-
 Light Photocatalysis in Nitrogen-Doped Titanium Oxides. *Science*
2001, *293*, 269–271.
- Di Valentin, C.; Finazzi, E.; Pacchioni, G.; Selloni, A.; Livarghi, S.;
 Paganini, M. C.; Giamello, E. N-Doped TiO₂: Theory and Experiment. *Chem. Phys.* **2007**, *339*, 44–56.
- Di Valentin, C.; Pacchioni, G.; Selloni, A. Origin of the Different
 Photoactivity of N-Doped Anatase and Rutile TiO₂. *Phys. Rev. B* **2004**,
70, 085116/1–085116/4.
- Barolo, G.; Livraghi, S.; Chiesa, M.; Paganini, M. C.; Giamello,
 E. Mechanism of the Photoactivity under Visible Light of N-Doped
 Titanium Dioxide. Charge Carriers Migration in Irradiated N-TiO₂
 Investigated by Electron Paramagnetic Resonance. *J. Phys. Chem. C*
2012, *116*, 20887–20894.
- Ceotto, M.; Lo Presti, L.; Cappelletti, G.; Meroni, D.;
 Spadavecchia, F.; Zecca, R.; Leoni, M.; Scardi, P.; Bianchi, C. L.;
 Ardizzone, S. About the Nitrogen Location in Nanocrystalline N-
 Doped TiO₂: Combined DFT and EXAFS Approach. *J. Phys. Chem. C*
2012, *116*, 1764–1771.
- Wu, G.; Nishikawa, T.; Ohtani, B.; Chen, A. Synthesis and
 Characterization of Carbon-Doped NiO Nanostructures with
 Enhanced Visible Light Response. *Chem. Mater.* **2007**, *19*, 4530–4537.

- (9) Park, J. H.; Kim, S.; Bard, A. J. Novel Carbon-Doped TiO₂ Nanotube Arrays with High Aspect Ratios for Efficient Solar Water Splitting. *Nano Lett.* **2006**, *6*, 24–28.
- (10) Di Valentin, C.; Pacchioni, G.; Selloni, A. Theory of Carbon Doping of Titanium Dioxide. *Chem. Mater.* **2005**, *17*, 6656–6665.
- (11) Graciani, J.; Ortega, Y.; Sanz, J. F. Carbon Doping of the TiO₂ (110) Rutile Surface. A Theoretical Study Based on DFT. *Chem. Mater.* **2009**, *21*, 1431–1438.
- (12) Wang, H.; Lewis, J. P. Second-Generation Photocatalytic Materials: Anion-Doped TiO₂. *J. Phys.: Condens. Matter* **2006**, *18*, 421–434.
- (13) Wang, H.; Lewis, J. P. Effects of Dopant States on Photoactivity in Carbon-Doped TiO₂. *J. Phys.: Condens. Matter* **2005**, *17*, L209–L214.
- (14) Di Valentin, C.; Pacchioni, G.; Onishi, H.; Kudo, A. Cr/Sb Co-Doped TiO₂ from First Principles Calculations. *Chem. Phys. Lett.* **2009**, *469*, 166–171.
- (15) Yu, J. G.; Xiang, Q. J.; Zhou, M. H. Preparation, Characterization and Visible-Light-Driven Photocatalytic Activity of Fe-Doped Titania Nanorods and First-Principles Study for Electronic Structures. *Appl. Catal., B* **2009**, *90*, 595–602.
- (16) Long, R.; English, N. J. First-Principles Calculation of Synergistic (N, P)-Codoping Effects on the Visible-Light Photocatalytic Activity of Anatase TiO₂. *J. Phys. Chem. C* **2010**, *114*, 11984–11990.
- (17) Zheng, J. W.; Bhattacharyya, A.; Wu, P.; Chen, Z.; Highfield, J.; Dong, Z. L.; Xu, R. The Origin of Visible Light Absorption in Chalcogen Element (S, Se, and Te)-Doped Anatase TiO₂ Photocatalysts. *J. Phys. Chem. C* **2010**, *114*, 7063–7069.
- (18) Peng, H. W.; Li, J. B.; Li, S. S.; Xia, J. B. First-Principles Study of the Electronic Structures and Magnetic Properties of 3d Transition Metal-Doped Anatase TiO₂. *J. Phys.: Condens. Matter* **2008**, *20*, 125207.
- (19) Bian, L.; Song, M. X.; Zhou, T. L.; Zhao, X. Y.; Dai, Q. Q. Band Gap Calculation and Photo Catalytic Activity of Rare Earths Doped Rutile TiO₂. *J. Rare Earths* **2009**, *27*, 461–468.
- (20) Kubacka, A.; Fernandez-Garcia, M.; Colon, G. Advanced Nanoarchitectures for Solar Photocatalytic Applications. *Chem. Rev.* **2012**, *112*, 1555–1614.
- (21) Primo, A.; Corma, A.; Garcia, H. Titania Supported Gold Nanoparticles as Photocatalyst. *Phys. Chem. Chem. Phys.* **2011**, *13*, 886–910.
- (22) Herrmann, J. M. Detrimental Cationic Doping of Titania in Photocatalysis: Why Chromium Cr³⁺-Doping is a Catastrophe for Photocatalysis, Both under UV- and Visible Irradiations. *New. J. Chem.* **2012**, *36*, 883–890.
- (23) Tada, H.; Mitsui, T.; Kiyonaga, T.; Akita, T.; Tanaka, K. All-Solid-State Z-Scheme in CdS–Au–TiO₂ Three-Component Heterojunction System. *Nat. Mater.* **2006**, *5*, 782–786.
- (24) Williams, G.; Seger, B.; Kamat, P. V. TiO₂-Graphene Nanocomposites. UV-Assisted Photocatalytic Reduction of Graphene Oxide. *ACS Nano* **2008**, *2*, 1487–1491.
- (25) Murakami, N.; Chiyoya, T.; Tsubota, T.; Ohno, T. Switching Redox Site of Photocatalytic Reaction on Titanium(IV) Oxide Particles Modified with Transition-Metal Ion Controlled by Irradiation Wavelength. *Appl. Catal., A* **2008**, *348*, 148–152.
- (26) Yu, H.; Irie, H.; Shimodaira, Y.; Hosogi, Y.; Kuroda, Y.; Miyauchi, M.; Hashimoto, K. An Efficient Visible-Light-Sensitive Fe(III)-Grafted TiO₂ Photocatalyst. *J. Phys. Chem. C* **2010**, *114*, 16481–16487.
- (27) Hong, S. J.; Lee, S.; Jang, J. S.; Lee, J. S. Heterojunction BiVO₄/WO₃ Electrodes for Enhanced Photoactivity of Water Oxidation. *Energy Environ. Sci.* **2011**, *4*, 1781–1787.
- (28) Kong, L.; Jiang, Z.; Xiao, T.; Lu, L.; Jones, M. O.; Edwards, P. P. Exceptional Visible-Light-Driven Photocatalytic Activity over BiOBr–ZnFe₂O₄ Heterojunctions. *Chem. Commun.* **2011**, *47*, 5512–5514.
- (29) Libera, J. A.; Elam, J. W.; Sather, N. F.; Rajh, T. M.; Dimitrijevic, N. M. Iron(III)-Oxo Centers on TiO₂ for Visible-Light Photocatalysis. *Chem. Mater.* **2010**, *22*, 409–413.
- (30) Tada, H.; Jin, Q.; Nishijima, H.; Yamamoto, H.; Fujishima, M.; Okuoka, S.-i.; Hattori, T.; Sumida, Y.; Kobayashi, H. Titanium(IV) Dioxide Surface-Modified with Iron Oxide as a Visible Light Photocatalyst. *Angew. Chem., Int. Ed.* **2011**, *50*, 3501–3505.
- (31) Jin, Q.; Fujishima, M.; Tada, H. Visible-Light-Active Iron Oxide-Modified Anatase Titanium(IV) Dioxide. *J. Phys. Chem. C* **2011**, *115*, 6478–6483.
- (32) Fujishima, M.; Jin, Q.; Yamamoto, H.; Tada, H.; Nolan, M. Tin Oxide-Surface Modified Anatase Titanium(IV) Dioxide with Enhanced UV-Light Photocatalytic Activity. *Phys. Chem. Chem. Phys.* **2012**, *14*, 705–711.
- (33) Jin, Q.; Fujishima, M.; Nolan, M.; Iwaszuk, A.; Tada, H. Photocatalytic Activities of Tin(IV) Oxide Surface-Modified Titanium(IV) Dioxide Show a Strong Sensitivity to the TiO₂ Crystal Form. *J. Phys. Chem. C* **2012**, *116*, 12621–12626.
- (34) Boppana, V. B. R.; Lobo, R. F. SnO_x-ZnGa₂O₄ Photocatalysts with Enhanced Visible Light Activity. *ACS Catal.* **2011**, *1*, 923–928.
- (35) Cheng, H.; Huang, B.; Dai, Y.; Qin, X.; Zhang, X. One-Step Synthesis of the Nanostructured AgI/BiOI Composites with Highly Enhanced Visible-Light Photocatalytic Performances. *Langmuir* **2010**, *26*, 6618–6624.
- (36) Murakami, N.; Chiyoya, T.; Tsubota, T.; Ohno, T. Switching Redox Site of Photocatalytic Reaction on Titanium(IV) Oxide Particles Modified with Transition-Metal Ion Controlled by Irradiation Wavelength. *Appl. Catal., A* **2008**, *348*, 148–152.
- (37) Jin, Q.; Ikeda, T.; Fujishima, M.; Tada, H. Nickel(II) Oxide Surface-Modified Titanium(IV) Dioxide as a Visible-Light-Active Photocatalyst. *Chem. Commun.* **2011**, *47*, 8814–8816.
- (38) Iwaszuk, A.; Nolan, M. Reactivity of Sub 1 nm Supported Clusters: (TiO₂)_n Clusters Supported on Rutile TiO₂ (110). *Phys. Chem. Chem. Phys.* **2011**, *13*, 4963–4973.
- (39) Nolan, M. Surface Modification of TiO₂ with Metal Oxide Nanoclusters: a Route to Composite Photocatalytic Materials. *Chem. Commun.* **2011**, *47*, 8617–8619.
- (40) Kresse, G.; Hafner, J. Ab Initio Molecular-Dynamics Simulation of the Liquid-Metal-Amorphous-Semiconductor Transition in Germanium. *Phys. Rev. B* **1994**, *49*, 14251–14269.
- (41) Blöchl, P. E. Projector Augmented-Wave Method. *Phys. Rev. B* **1994**, *50*, 17953–17979.
- (42) Perdew, J. P. In *Electronic Structure of Solids '91*; Ziesche, P., Eschrig, H., Eds.; Akademie Verlag: Berlin, Germany, 1991.
- (43) Diebold, U. The Surface Science of Titanium Dioxide. *Surf. Sci. Rep.* **2003**, *48*, 53–229.
- (44) Liu, M.; Piao, L.; Zhao, L.; Ju, S.; Yan, Z.; He, T.; Zhou, C.; Wang, W. Anatase TiO₂ Single Crystals with Exposed {001} and {110} Facets: Facile Synthesis and Enhanced Photocatalysis. *Chem. Commun.* **2010**, *46*, 1664–1666.
- (45) Yang, W.; Li, J.; Wang, Y.; Zhu, F.; Shi, W.; Wan, F.; Xu, D. A Facile Synthesis of Anatase TiO₂ Nanosheets-Based Hierarchical Spheres with over 90% {001} Facets for Dye-Sensitized Solar Cells. *Chem. Commun.* **2011**, *47*, 1809–1811.
- (46) Anisimov, V. I.; Zaanen, J.; Andersen, O. K. Band Theory and Mott Insulators: Hubbard U instead of Stoner I. *Phys. Rev. B* **1991**, *44*, 943–954.
- (47) Dudarev, S. L.; Botton, G. A.; Savrasov, S. Y.; Humphreys, C. J.; Sutton, A. P. Electron-Energy-Loss Spectra and the Structural Stability of Nickel Oxide: An LSDA+U Study. *Phys. Rev. B* **1998**, *57*, 1505–1509.
- (48) Morgan, B. J.; Watson, G. W. A DFT+U Description of Oxygen Vacancies at the TiO₂ Rutile (110) Surface. *Surf. Sci.* **2007**, *601*, 5034–5041.
- (49) Ganduglia-Pirovano, M. V.; Hofmann, A.; Sauer, J. Oxygen Vacancies in Transition Metal and Rare Earth Oxides: Current State of Understanding and Remaining Challenges. *Surf. Sci. Rep.* **2007**, *62*, 219–270.
- (50) Nolan, M.; Grigoleit, S.; Sayle, D. C.; Parker, S. C.; Watson, G. W. Density Functional Theory Studies of the Structure and Electronic Structure of Pure and Defective Low Index Surfaces of Ceria. *Surf. Sci.* **2005**, *576*, 217–229.

- 734 (51) Ferrari, A. M.; Pisani, C.; Cincini, F.; Giordano, L.; Pacchioni,
735 G. Cationic and Anionic Vacancies on the NiO(100) Surface: DFT+U
736 and Hybrid Functional Density Functional Theory Calculations. *J.*
737 *Chem. Phys.* **2007**, *127*, 174711.
- 738 (52) Long, R.; English, N. J.; Mooney, D. A. Electronic Structures of
739 N- and C-Doped NiO from First-Principles Calculations. *Phys. Lett. A*
740 **2010**, *374*, 1184–1187.
- 741 (53) Yu, N.; Zhang, W.-B.; Wang, N.; Wang, W.-F.; Tang, B.-Y.
742 Water Adsorption on a NiO(100) Surface: A GGA+U Study. *J. Phys.*
743 *Chem. C* **2008**, *112*, 452–457.
- 744 (54) Tada, H.; Matsui, H.; Shiota, F.; Nomura, M.; Ito, S.; Yoshihara,
745 M.; Esumi, K. Heterosupramolecular Photocatalysis: Oxidation of
746 Organic Compounds in Nanospaces between Surfactant Bilayers
747 Formed on TiO₂. *Chem. Commun.* **2002**, 1678–1679.
- 748 (55) Nolan, M.; Iwaszuk, A.; Tada, H. Molecular Metal Oxide
749 Cluster-Surface Modified Titanium(IV) Dioxide Photocatalysts. *Aust.*
750 *J. Chem.* **2012**, *65*, 624–632.
- 751 (56) Niishiro, R.; Kato, H.; Kudo, A. Nickel and Either Tantalum or
752 Niobium-Codoped TiO₂ and SrTiO₃ Photocatalysts with Visible-Light
753 Response for H₂ or O₂ Evolution from Aqueous Solutions. *Phys. Chem.*
754 *Chem. Phys.* **2005**, *7*, 2241–2245.
- 755 (57) Liu, G.; Wang, L.; Yang, H. G.; Cheng, H. -M.; Lu, G. Q.
756 Titania-Based Photocatalysts—Crystal Growth, Doping and Hetero-
757 structuring. *J. Mater. Chem.* **2010**, *20*, 831–843.
- 758 (58) Serpone, N.; Lawless, D.; Khairutdinov, R. Size Effects on the
759 Photophysical Properties of Colloidal Anatase TiO₂ Particles: Size
760 Quantization versus Direct Transitions in This Indirect Semi-
761 conductor. *J. Phys. Chem.* **1995**, *99*, 16646–16654.
- 762 (59) Anpo, M.; Takeuchi, M. The Design and Development of
763 Highly Reactive Titanium Oxide Photocatalysts Operating under
764 Visible Light Irradiation. *J. Catal.* **2003**, *216*, 505–516.
- 765 (60) Kitano, M.; Funatsu, K.; Matsuoka, M.; Ueshima, M.; Anpo, M.
766 Preparation of Nitrogen-Substituted TiO₂ Thin Film Photocatalysts by
767 the Radio Frequency Magnetron Sputtering Deposition Method and
768 Their Photocatalytic Reactivity under Visible Light Irradiation. *J. Phys.*
769 *Chem. B* **2006**, *110*, 25266–25272.
- 770 (61) Nolan, M.; Tofail, S. A. M. Density Functional Theory
771 Simulation of Titanium Migration and Reaction with Oxygen in the
772 Early Stages of Oxidation of Equiatomic NiTi alloy. *Biomaterials* **2010**,
773 *31*, 3439–3448.
- 774 (62) Henkelman, G.; Arnaldsson, A.; Jónsson, H. A Fast and Robust
775 Algorithm for Bader Decomposition of Charge Density. *Comput.*
776 *Mater. Sci.* **2006**, *36*, 354–360.
- 777 (63) Wang, C. M.; Heller, A.; Gerischer, H. Palladium Catalysis of O₂
778 Reduction by Electrons Accumulated on TiO₂ Particles during
779 Photoassisted Oxidation of Organic Compounds. *J. Am. Chem. Soc.*
780 **1992**, *114*, 5230–5234.
- 781 (64) Hoffmann, M. R.; Martin, S. T.; Choi, W.; Bahnemann, D. W.
782 Environmental Application of Semiconductor Photocatalysis. *Chem.*
783 *Rev.* **1995**, *95*, 69–96.